*energies*

MDPI

*Article*

# Joint Planning of Renewable Energy and Electric Vehicle Charging Stations Based on a Carbon Pricing Optimization Mechanism

**Shanli Wang [1], Bing Fang [1], Jiayi Zhang [1], Zewei Chen [1], Mingzhe Wen [1], Huanxiu Xiao [1] and Mengyao Jiang [2,*]**

[1] Hainan Power Grid Co., Ltd., Haikou 570203, China
[2] Institute of New Energy, Wuhan 430206, China
* Correspondence: daisy_jiang17@163.com

**Abstract**

The integration of renewable energy and electric vehicle (EV) charging stations into distribution systems presents critical challenges, including the inherent variability of renewable generation, the complex behavioral patterns of EV users, and the need for effective carbon emission mitigation. To address these challenges, this paper proposes a novel distribution system planning method based on the carbon pricing optimization mechanism. First, to address the strong randomness and volatility of renewable energy, a prediction model for renewable energy output considering climatic conditions is established to characterize the output features of wind and solar power. Subsequently, a charging station model is constructed based on the behavioral characteristics of electric vehicle users. Then, an optimized carbon trading price mechanism incorporating the carbon price growth rate is introduced into the carbon emission cost accounting. Based on this, a joint planning model for the power and transportation systems is developed, aiming to minimize the total economic cost while accounting for renewable energy integration and electric vehicle charging station deployment. In the case study, the proposed model is validated using the actual operational data of a specific region and a modified IEEE 33-node system, demonstrating the rationality and effectiveness of the model.

**Keywords:** CEEMDAN-LSTM; output forecast; EV charging station site selection; optimizing the carbon trading pricing mechanism

check for updates

Academic Editor: Tek Tjing Lie

Received: 19 May 2025
Revised: 27 June 2025
Accepted: 27 June 2025
Published: 1 July 2025

**Citation:** Wang, S.; Fang, B.; Zhang, J.; Chen, Z.; Wen, M.; Xiao, H.; Jiang, M. Joint Planning of Renewable Energy and Electric Vehicle Charging Stations Based on a Carbon Pricing Optimization Mechanism. *Energies* **2025**, *18*, 3462. https://doi.org/10.3390/en18133462

**Copyright:** © 2025 by the authors. Licensee MDPI, Basel, Switzerland. This article is an open access article distributed under the terms and conditions of the Creative Commons Attribution (CC BY) license (https://creativecommons.org/licenses/by/4.0/).

## 1. Introduction

The rapid global adoption of renewable energy and electric vehicles (EVs) presents both opportunities and challenges for modern power systems [1]. While wind and solar generation capacity has grown exponentially, their inherent intermittency and spatiotemporal variability complicate grid planning and operation, necessitating high-precision forecasting methods to mitigate uncertainty. Concurrently, EV adoption introduces aggregated charging loads with distinct temporal patterns, further straining distribution networks. Compounding these challenges, carbon pricing frameworks have emerged as critical policy tools to incentivize decarbonization, yet existing mechanisms often lack the flexibility to adapt to dynamic emission reduction targets [2]. This trend has forced the comprehensive upgrade of the distribution network planning concepts and methods, and it is urgent to build a new planning system that adapts to the high proportion of renewable energy access. Modern distribution network planning has evolved into a multidimensional, multi-stage system of engineering, and its core tasks can be decomposed into power supply side collaborative planning and grid planning [3]. Power planning is no longer limited

to the site selection and capacity determination of traditional thermal power plants and gas turbines. Still, it needs to comprehensively consider the penetration rate of fluctuating power sources such as wind and solar power, the clustering effect of distributed energy, and the optimal configuration of flexible resources such as charging piles and energy storage power stations [4]. The planning focus has shifted from simple capacity matching to both "controllability" and "flexibility" to ensure that the system can still operate stably when the output of renewable energy fluctuates greatly [5]. Grid planning improves the carrying capacity and fault self-healing ability of the existing network through line capacity expansion and intelligent segmented switch deployment. For application scenarios such as emerging industrial parks, a new topology is constructed, and access space for technologies such as energy storage is reserved [6–8]. From passively adapting to load growth to actively guiding energy transformation and upgrading, the maximum absorption of renewable energy is achieved while ensuring power supply reliability.

In the context of new power systems, the volatility and spatiotemporal uncertainty of renewable energy represented by photovoltaic and wind power have significantly increased the planning difficulty of distribution networks in terms of grid optimization, operation scheduling, and improvement of absorption capacity. High-precision renewable energy output forecasts (such as wind speed and solar irradiance) are the core inputs for planning decisions, and their reliability is directly related to the economic performance and stability of the power system [9]. Existing prediction methods primarily fall into three categories: ① Traditional statistical models: These mainly include the primary approach, which involves time series forecasting based on the auto-regressive moving average (ARMA) model, and hybrid prediction methods based on seasonal and trend decomposition using LOESS (STL) decomposition and simple exponential smoothing (SES) [10,11]. This type of method achieves trend fitting through linear assumptions and periodic decomposition, but it is not capable of capturing nonlinear characteristics (such as power mutations caused by extreme weather) and is difficult to handle multivariate coupling relationships; ② Traditional machine learning methods: Techniques such as support vector machines (SVM) [12], random forests, and gradient boosting decision trees (GBDT) [13] can improve nonlinear fitting through feature engineering. However, they suffer from inherent limitations in temporal dependency modeling, and the manual feature construction process may introduce subjective biases, leading to high computational complexity and poor real-time performance. ③ Deep learning models: These include convolutional neural networks (CNN) [14], transformer [15], and long short-term memory (LSTM). Although LSTM excels in temporal modeling, standalone LSTM algorithms [16] exhibit limited capability in modeling non-stationary signals (e.g., abrupt changes in solar irradiance or wind speed). Moreover, traditional decomposition methods like empirical mode decomposition (EMD) may obscure the physical interpretability of subsequences, further compromising prediction reliability.

As the penetration rate of EV charging load in the power system continues to rise, its agglomeration characteristics in time and space dimensions have a profound impact on the planning and operation of the distribution network [17]. Scientific modeling and in-depth analysis are needed at the system level to ensure the safety, reliability, and economy of the power grid [18]. According to the differences in charging behavior, EV users can be divided into two categories [19]: slow-charging users (mainly private cars, charging at fixed time periods at night in residential areas) and fast-charging users (mainly taxis, relying on centralized fast-charging stations for high-frequency short-term charging). Since the access location of centralized fast-charging stations directly affects the distribution of the distribution network power flow, their site selection and capacity determination must be based on refined load forecasting. Existing EV load forecasting methods mainly

include the following: ① Probabilistic modeling method: constructing charging demand probability distribution based on historical data (such as Monte Carlo simulation) [20,21]. It has high computational efficiency but tends to ignore user dynamic behavior. ② Travel behavior analysis method: inferring load demand through the transmission relationship and transmission rules between user activity chains combined with a dynamic traffic distribution model [22]. Although it can reflect individual behavior logic, it is difficult to extend to the entire user group. ③ Data-driven method: using travel trajectory data for data mining and integrated modeling to predict load results [23,24]. Although this method has strong timeliness, it relies on high-cost data collection systems. Current research mostly integrates EV loads and lacks modeling of differentiated charging modes for slow-charging/fast-charging users, resulting in prediction results that are difficult to support differentiated distribution network planning needs.

As the types of loads such as distributed energy and electric vehicles continue to increase, distribution network planning has begun to shift from considering single elements such as power supply reliability and flexibility [25] and network losses [26] to a new distribution network that integrates multiple elements such as distributed power sources and electric vehicles. Reference [27] proposed a joint planning method for electric vehicle charging stations and distribution networks, which considered the demand characteristics of charging stations. Reference [28] incorporated distributed power sources into distribution network planning and proposed a distribution network planning method based on probabilistic flow, using a probabilistic model to deal with the large number of uncertainties brought about by wind power and photovoltaic access. To meet the demand for maximizing renewable energy accommodation, distribution network planning must also account for the impact of carbon emissions to achieve sustainable development. Reference [29] incorporated carbon emission costs into distribution network planning to reduce greenhouse gas emissions. However, the carbon emission model employed was overly simplistic and failed to consider the positive role of carbon trading markets in incentivizing emission reductions. Reference [30] introduced a carbon trading mechanism by incorporating the carbon price as a fixed parameter within the carbon cost objective of the operational model. However, this approach overlooked the temporal variability of carbon prices and the tradability of carbon allowances, resulting in a relatively rigid representation of the carbon market. Consequently, it failed to adequately reflect the dynamic nature and complexity of real-world carbon trading mechanisms. To address such limitations, Reference [31] presented a traditional tiered carbon trading mechanism alongside a carbon emission calculation model. In this framework, the carbon price increases stepwise with the quantity of emission allowances purchased, strengthening cost signals for higher emissions. Nevertheless, its pricing structure remains static and lacks adaptability to real-time emission dynamics. Building upon this, Reference [32] improved the model by introducing a carbon price growth rate, enabling the carbon price to increase progressively across emission stages. This enhancement not only added flexibility to the pricing mechanism but also improved its effectiveness in incentivizing emission reductions and aligning carbon pricing with actual emission behaviors.

The rapid integration of renewable energy and EVs introduces critical challenges for power systems, including renewable intermittency, spatially concentrated EV charging loads, and inefficient carbon pricing mechanisms. Existing planning approaches often address these issues in isolation, failing to capture their interdependencies. This paper proposes a power grid planning method incorporating renewable energy and EV charging stations, leveraging a carbon pricing optimization mechanism. The key innovations include the following: (1) A renewable energy output prediction model considering climatic conditions is established to characterize the generation profiles of wind and solar power. (2) EV

users are categorized into slow-charging and fast-charging users based on differences in charging behavior. Queueing theory and probabilistic forecasting models are employed to simulate travel patterns and analyze charging demand, thereby constructing an accurate charging station model. (3) A more flexible and incentive-driven carbon pricing optimization mechanism is introduced by incorporating carbon price growth rate adjustments, facilitating the efficient allocation of clean energy resources and dynamic optimization of carbon emission reduction pathways. Building upon this framework, an integrated power-traffic system co-planning model is formulated, minimizing total economic costs while accounting for renewable energy siting, EV charging station spatial distribution, and carbon trading expenses.

The remainder of this paper is structured as follows. In renewable energy forecasting, Section 2 adopts a hybrid strategy combining complete ensemble empirical mode decomposition with adaptive noise (CEEMDAN) and multi-channel LSTM networks, significantly enhancing the accuracy and robustness of wind and photovoltaic power predictions. This provides more reliable data support for subsequent optimization. In Section 3, the heterogeneity of user behavior is rigorously addressed for EV load modeling: queueing theory models are applied to fast-charging users, while probabilistic forecasting models are developed for slow-charging users. This granular approach improves the realism and specificity of charging load predictions, enabling more targeted charging station deployment. In Section 4, the innovative integration of carbon price growth rate optimization enhances the flexibility and incentivization of the carbon pricing mechanism design. This promotes rational integration of distributed renewable energy and strengthens the system-wide carbon emission reduction capability. A case study based on the IEEE 33-node system is presented in Section 5. The conclusion and discussion are provided in Section 6 and Section 7, respectively.

## 2. Renewable Energy Output Forecasting Based on CEEMDAN-LSTM

When describing the output characteristics of wind power and photovoltaic power, traditional methods usually directly use the light intensity curve and wind speed curve of a certain area for modeling. However, this method ignores the potential impact of environmental factors (such as temperature, humidity, air pressure, etc.) on wind power and photovoltaics, which may lead to deviations between the predicted results and the actual output. To more accurately characterize the output characteristics of renewable energy, this paper first conducts data-driven modeling of wind speed and light intensity based on historical data of multidimensional meteorological parameters, including wind speed, light intensity, temperature, humidity, and air pressure, and uses the CEEMDAN-LSTM algorithm for time series forecasting to improve the forecast accuracy and optimize the planning of renewable energy [33].

### *2.1. CEEMDAN Decomposition*

Ensemble empirical mode decomposition (EEMD) introduces random noise to the original data, performs EMD decomposition, and then takes the average [34,35]. The EEMD method can significantly alleviate the common modal aliasing problem in the EMD method by improving the decomposition process and improving the reliability of the decomposition results. The complete ensemble empirical mode decomposition (CEEMD) algorithm adds a large amount of Gaussian white noise with opposite phases and the same amplitude to the reconstructed signal based on EEMD. The decomposed and synthesized signal not only solves the problem of modal aliasing, but also keeps the residual noise value at a small level [36].

The CEEMDAN algorithm is further optimized based on CEEMD, which enhances the stability and accuracy of decomposition. This method adds a limited number of

adaptive white noises, which not only reduces the calculation time but also reduces the reconstruction error [37]. The steps of CEEMDAN to process the meteorological data sequence are as follows:

(1) Assume that the white noise sequence $v^i(t)$ added for the $i$-th time obeys the normal distribution, the signal-to-noise ratio is represented by $\varepsilon_k$, and the operator of the $k$-th IMF generated by the EMD algorithm is $E_k(*)$. The meteorological data sequence after the $i$-th noise is recorded as $x^i(t)$, and its calculation formula is as follows:

$$x^i(t) = x(t) + \varepsilon_0 v^i(t) \tag{1}$$

where $i$ represents the number of experiments conducted, $i$ = 1,2, . . ., $I$, and $\varepsilon_0$ means the signal-to-noise ratio during the first decomposition stage.

(2) The EMD algorithm is applied to each noisy meteorological data sequence for decomposition processing, and then all modal components are summed and averaged to obtain the first modal component $\mathrm{IMF}_1(t)$ and the residual component $R_1(t) = x(t) - \mathrm{IMF}_1(t)$.

(3) Continue to decompose $R_1(t) + \varepsilon_1 E_1[v^i(t)]$ once more to obtain the second IMF of CEEMDAN, namely,

$$\mathrm{IMF}_2 = \frac{1}{I}\sum_{i=1}^{I} E_1\left\{R_1(t) + \varepsilon_1 E_1[v^i(t)]\right\} \tag{2}$$

where $\varepsilon_1$ means the signal-to-noise ratio during the second decomposition stage.

(4) The calculation of the $(k + 1)$th IMF and residual component is the same as Step 3, expressed as follows:

$$R_{k+1}(t) = R_k(t) - IMF_{k+1}(t) \tag{3}$$

$$\mathrm{IMF}_{k+1} = \frac{1}{I}\sum_{i=1}^{I} E_k\left\{R_k(t) + \varepsilon_k E_k[v^i(t)]\right\} \tag{4}$$

(5) Until all residual components cannot be further decomposed, and the extreme value of the residual component is less than or equal to 2, the final residual component is as follows:

$$R(t) = x(t) - \sum_{k=1}^{K} \mathrm{IMF}_k \tag{5}$$

The signal time series is decomposed into the following:

$$x(t) = \sum_{k=1}^{K} \mathrm{IMF}_k + R(t) \tag{6}$$

According to the above steps, it is found that the appropriate signal-to-noise ratio can be selected through the coefficient $\varepsilon_k$ during decomposition; the reconstruction accuracy of the original meteorological data sequence is higher, and the calculation amount is less. The block diagram of CEEMDAN is shown in Figure 1.

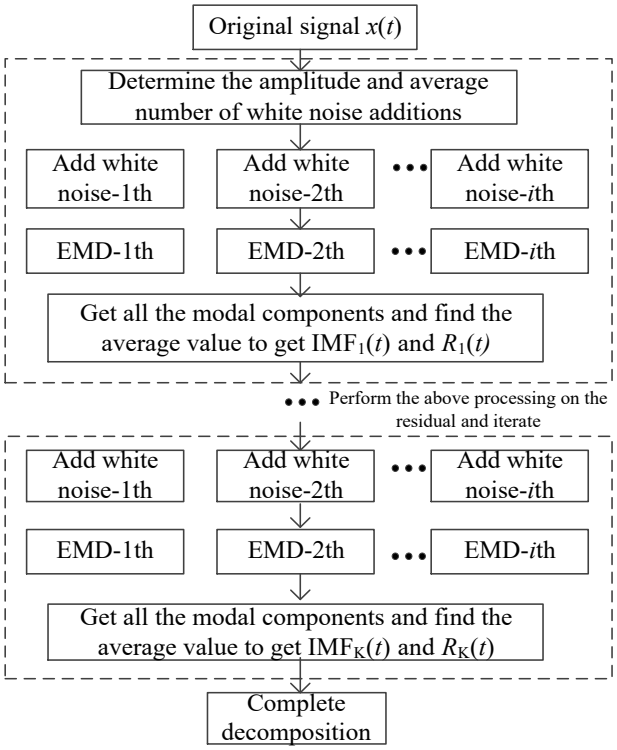


**Figure 1.** CEEMDAN block diagram.

### *2.2. LSTM Prediction Model*

The LSTM model consists of multiple gate structures, including an input gate, an output gate, and a forget gate, which work together to dynamically adjust the transmission and retention of information. As an improved form of a recurrent neural network, the LSTM model is good at capturing long-term dependencies and nonlinear trends in time series through the gating mechanism. Renewable energy is highly volatile and has time-series dependencies. LSTM can effectively alleviate the gradient vanishing problem and is suitable for processing wind speed and light intensity prediction tasks with multidimensional input. The structure of LSTM is shown in Figure 2.

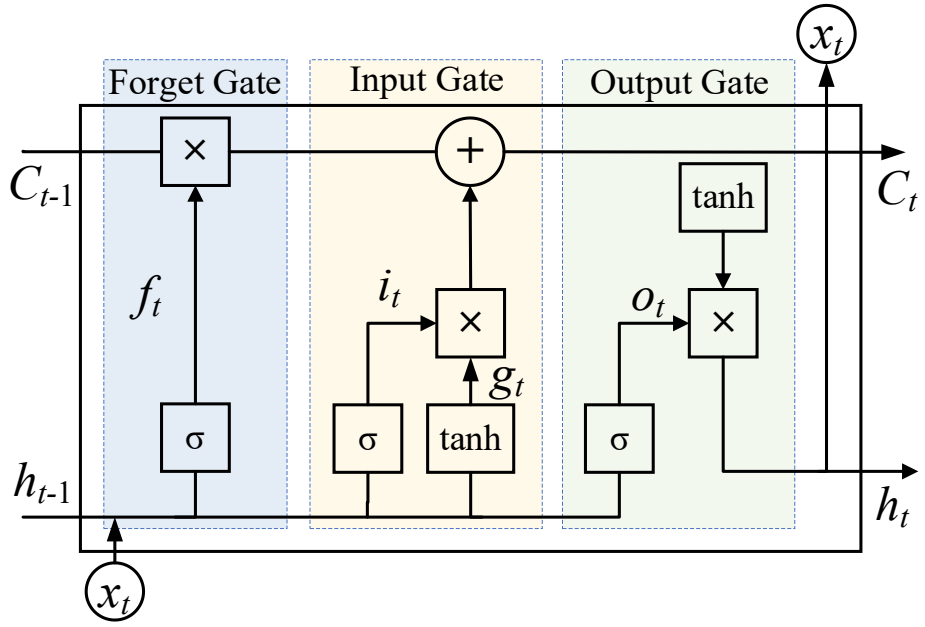


**Figure 2.** Diagram of LSTM internal structure.

The core of the LSTM model is the process from the old memory state $C_{t-1}$ to the new memory state $C_t$. The algorithm uses a gate mechanism to memorize important information. The forgotten features in $C_{t-1}$ are obtained by the forget gate $f_t$, which stops the forgotten features from entering the subsequent processing flow. $f_t$ is a vector with elements ranging from [0,1]. $\otimes$ indicates that there is a unit multiplication relationship between $C_{t-1}$ and $f_t$. The internal operation process of the LSTM unit is as Equations (7)–(12).

The forget gate $f_t$ is shown as follows:

$$f_t = \sigma(W_f \cdot [h_{t-1}, x_t] + b_f) \tag{7}$$

The input gate $i_t$ is shown as follows:

$$i_t = \sigma(W_i \cdot [h_{t-1}, x_t] + b_i) \tag{8}$$

The summarized status value $\widetilde{C}_t$ is shown as follows:

$$\widetilde{C}_t = \tanh(W_c \cdot [h_{t-1}, x_t] + b_c) \tag{9}$$

The new memory state $C_t$ is shown as follows:

$$C_t = f_t \times C_{t-1} + i_t \times \widetilde{C}_t \tag{10}$$

In the formula, $i_t$ is the input gate. Both $i_t$ and $f_t$ are vectors with elements between [0,1] and are obtained by the input data $x_t$ and the previous hidden state $h_{t-1}$ through the sigmoid activation function. $x_t$ and $h_t$ are obtained through the tanh activation function.

The output gate $O_t$ is shown as follows:

$$O_t = \sigma(W_o \cdot [h_{t-1}, x_t] + b_O) \tag{11}$$

The updated output $h_t$ is shown as follows:

$$h_t = O_t * \tanh(C_t) \tag{12}$$

In the formula, $\sigma$ represents the sigmoid activation function, tanh represents the hyperbolic tangent function, $W_f$, $W_i$, $W_c$, and $W_o$ are weight matrices, and $b_f$, $b_i$, $b_c$, and $b_o$ are bias terms. The optimal model is obtained by optimizing the input data through multiple cycles.

### *2.3. Wind Power Output and Photovoltaic Output Forecast*

This paper selects relevant historical data from a certain place as the test dataset. The time resolution of this data set is 1 h, and it contains five key meteorological indicators: wind speed, light intensity, temperature, humidity, and air pressure. Although solar irradiance is the most direct input to determine the photovoltaic output prediction, other meteorological parameters play an important synergistic role in the CEEMDAN-LSTM model. Temperature directly affects the conversion efficiency of photovoltaic cells. The power output of silicon photovoltaic cells decreases with the increase in temperature. High humidity will increase the content of water vapor in the atmosphere and reduce the actual solar radiation intensity reaching photovoltaic modules. The change in air pressure is closely related to the weather system, which affects the scattering and absorption of solar radiation due to large air tightness. Wind speed affects the temperature of photovoltaic modules through a cooling effect. Higher wind speed helps to reduce the temperature of modules and improve power generation efficiency. Therefore, we retain the five-dimensional meteorological characteristics in the CEEMDAN-LSTM framework, so that the network can capture the

nonlinear interaction between the parameters. This multi-parameter collaborative prediction method is more accurate than the traditional model that simply depends on the light intensity, especially in complex weather conditions, which can provide more reliable prediction results. The same is true for wind power output prediction.

The specific process of implementing the wind power and photovoltaic output model based on CEEMDAN-LSTM is as follows:

First, the data are preprocessed. Historical data are selected to construct a training set and normalized to eliminate the influence of different dimensions.

$$z' = \frac{z - z_{\min}}{z_{\max} - z_{\min}} \tag{13}$$

where $z'$ represents the normalized value, $z$ represents the original value, and $z_{\min}$ and $z_{\max}$ represent the minimum and maximum values, respectively.

The original data are decomposed into multiple subsequences and a residual term by using the CEEMDAN algorithm, thereby extracting different characteristic components of the signal.

The processed data are input into the LSTM neural network for iterative training to optimize the model parameters.

The test set data are input into the trained model to obtain the prediction results. The output data are denormalized and restored to the actual physical quantity. The root mean square error (RMSE), mean absolute error (MAE), and symmetric mean absolute percentage error (SMAPE) of the prediction results are calculated to evaluate the prediction accuracy.

The predicted wind speed and light intensity results are introduced into the Weibull distribution model and the photovoltaic Beta distribution model to calculate the output characteristics of wind power and photovoltaic power, respectively [38].

## 3. Modeling of the Power Distribution System Including Electric Vehicle Charging Stations

### *3.1. Electric Vehicle Charging Station Model*

This paper studies the electric vehicle load in the power supply area, which mainly includes two typical user groups: fast charging and slow charging. Among them, fast-charging users are mainly operating vehicles such as electric taxis, which use a high-power DC fast-charging mode. The charging behavior is concentrated in large public charging stations, with the characteristics of random charging time, large power demand, and short duration. Slow-charging users are mainly private passenger cars, which usually use AC slow charging. The charging period is highly concentrated in residential areas at night, showing obvious regularity.

#### 3.1.1. Fast-Charging EV User

The probability distribution of the fast-charging user arrival condition is a Poisson distribution, and the charging process can be modeled using the M/G/k model in queuing theory. In the M/G/k model, "M" represents the Markov arrival process, i.e., the Poisson distribution, which is highly consistent with the stochastic characteristics of the actual electric taxi arrivals at the charging station. Secondly, the charging duration is affected by factors such as the initial SOC of the battery, the charging power curve, and the user's midway departure. It presents a normal or lognormal non-exponential distribution and needs to be described by the general distribution (G). The "k" corresponds to k charging points in the charging station. The M/G/k model has obvious advantages in describing the fast-charging scenario of electric taxis, and it is an appropriate choice to describe the charging behavior of fast-charging users.

The Poisson distribution parameter $\xi$ is as follows:

$$\xi = \frac{N_{taxi}}{t_e} \tag{14}$$

where $N_{taxi}$ is the number of electric taxis in the centralized charging service area; and $t_e$ is the shift duration of electric taxis.

The calculation formula for a fast-charging user's charging time is as follows:

$$T = \frac{C_{FCN} - C_{FC,\mathrm{k}}}{P_{FCN}} \tag{15}$$

where $T$ is the charging time of the fast-charging user; $C_{FCN}$ is the rated battery capacity of the fast-charging user; $C_{FC,\mathrm{k}}$ is the remaining power of the k-th fast-charging user; and $P_{FCN}$ is the rated charging power of the fast charging in the charging station.

#### 3.1.2. Slow-Charging EV User

The probability density function of the charging initiation time, determined by the last return time, is as follows [39,40]:

$$f_s(s) = \begin{cases} \frac{1}{\sigma_s\sqrt{2\pi}} \exp[-\frac{(s-\mu_s)^2}{2\sigma_s^2}], (\mu_s - 12) < s \leq 24 \\ \frac{1}{\sigma_s\sqrt{2\pi}} \exp[-\frac{(s+24-\mu_s)^2}{2\sigma_s^2}], 0 < s \leq (\mu_s - 12) \end{cases} \tag{16}$$

where $s$ is the initial charging time, and $\mu_s$, $\sigma_s$ denote its expected value and standard deviation, respectively. $\mu_s$ = 17.6, $\sigma_s$ = 3.4.

The probability density function of daily mileage is as follows:

$$f_D = \frac{1}{x\sigma_D\sqrt{2\pi}} \exp[-\frac{(\ln x - \mu_D)^2}{2\sigma_D^2}] \tag{17}$$

where $x$ is the mileage, and $\mu_D$ is the mathematical expectation of the mileage. $\mu_D$ = 0.8.

Analogous to the variation in engine displacement among conventional fuel vehicles, this study considers the distribution of battery capacities in slow-charging electric vehicles, assuming a uniform distribution within the range of 20 to 30 kWh. Based on this assumption, and considering a constant charging rate of 0.1 C, the corresponding charging power $p$ is also assumed to follow a uniform distribution between 2 and 3 kW, reflecting the proportional relationship with battery capacity. Specifically, the probability density function of $p$ can be obtained as follows:

$$f_p(x) = \begin{cases} 1, & x \in [2,3] \\ 0, & other \end{cases} \tag{18}$$

The probability density function of the charging time can be obtained as follows:

$$f_{T_c} = \frac{1}{1.61 \times 0.15} \int_2^3 \frac{1.61 \times 0.15}{x\sigma_D\sqrt{2\pi}} \times \exp[-\frac{(\ln x - \ln 1.61 - \ln 0.15 + \ln p - \mu_D)^2}{2\sigma_D^2}] dp, x > 0 \tag{19}$$

Assuming that the charging process of electric vehicles is a constant power process, the total charging power of fast-charging users and slow-charging users of electric vehicles in period $t$ is as follows:

$$P_{EV,\mathrm{t}} = \sum_{k=1}^{N_{FC,t}} \frac{P_{FC,k,t}}{\eta_{FC}} + \sum_{k=1}^{N_{SC,t}} \frac{P_{SC,k,t}}{\eta_{SC}} \tag{20}$$

$$P_{FC,k,t} = P_{FCN}\varsigma_{FC,k,t} \tag{21}$$

$$P_{SC,k,t} = P_{SCN}\varsigma_{SC,k,t} \tag{22}$$

where $P_{FC,k,t}$ and $P_{SC,k,t}$ represent the charging power of the $k$-th fast-charging and slow-charging user at time $t$, respectively. $\eta_{FC}$ and $\eta_{SC}$ denote the charging efficiency of fast and slow chargers within the EV charging station, respectively. $P_{FCN}$ and $P_{SCN}$ are the rated charging power of the fast and slow chargers, respectively. $\varsigma_{FC,k,t}$ and $\varsigma_{SC,k,t}$ are binary state variables (ranging from 0 to 1), indicating the charging status of the $k$-th fast-charging and slow-charging user at time $t$; a value of 1 denotes that charging is in progress, and 0 otherwise.

### *3.2. Comprehensive Model for Distribution System Planning*

When electric vehicles are connected to the power system, the power system will have a new electric vehicle charging load and will work in coordination with renewable energy power generation equipment (such as wind power and photovoltaics). The overall model is as follows:

$$P_{G,j,t} = P_{MT,j,t} + P_{ESS,j,t} + P_{DG,j,t} \tag{23}$$

$$P_{L,j,t} = P_{EV,j,t} + P_{Load,j,t} \tag{24}$$

$$P_{j,t} = -P_{G,j,t} + P_{Load,j,t} \tag{25}$$

where $P_{G,j,t}$ denotes the active power output of the power source connected to node $j$ at time $t$; $P_{MT,j,t}$ is the MT output power of node $j$ in period $t$; $P_{ESS,j,t}$ represents the energy storage output power at node $j$ during time $t$; $P_{DG,j,t}$ is the output power of renewable energy at node $j$ during time $t$; $P_{L,j,t}$ refers to the active power consumption at node $j$ during time $t$; $P_{EV,j,t}$ is the total power consumed by fast-charging users and slow-charging users of electric vehicles connected to node $j$ during time $t$; $P_{Load,j,t}$ represents the load power at node $j$ during time $t$; and $P_{j,t}$ is the net nodal power at node $j$ during time $t$.

## 4. Comprehensive Cost Minimization Planning Model and Solution Considering the Carbon Price Growth Rate

### *4.1. Objective Function*

This paper considers multiple factors such as distribution network, renewable energy, and electric vehicle charging stations in the planning area, and establishes a comprehensive cost minimization planning model that takes into account investment cost, operation and maintenance cost, electricity purchase cost, and carbon emission cost.

$$C_{\min} = C_1 + C_2 + C_3 + C_4 \tag{26}$$

where $C_1$ is the annual electricity purchase cost; $C_2$ is the annual investment and construction cost; $C_3$ is the annual operation and maintenance cost; and $C_4$ is the annual carbon emission cost.

#### 4.1.1. Annual Electricity Purchase Cost $C_1$

$$C_1 = 365\rho(t)\sum_{t=1}^{T}(P_{loss,t} + P_{NET,t}) \tag{27}$$

where $\rho(t)$ is the unit time-of-use electricity price; $P_{loss,t}$ is the network loss in period $t$; and $P_{NET,t}$ is the interaction power between the distribution network and the main grid.

4.1.2. Annual Investment and Construction Cost $C_2$

$$C_2 = \lambda(C_{DG1} + C_{EV1} + C_{MT1} + C_{ESS1}) \tag{28}$$

where $C_{DG1}$ is the investment cost of renewable energy, $C_{EV1}$ is the investment cost of electric vehicle charging station, $C_{MT1}$ is the investment cost of gas turbine, $C_{ESS1}$ is the investment cost of energy storage power station, and $\lambda$ is the depreciation rate.

$$\lambda = \frac{a(1+a)^y}{(1+a)^y - 1} \tag{29}$$

where $a$ is the discount rate and $y$ is the useful life of the equipment.

1. The investment cost of an electric vehicle charging station

$$C_{EV1} = n_{EV}\gamma_{EV} + C_{EV\text{con}} \tag{30}$$

where $n_{EV}$ is the number of electric vehicle charging piles, $\gamma_{EV}$ is the purchase cost of a single charging pile, and $C_{EV\text{con}}$ is the fixed investment cost of the charging station.

2. The investment cost of distributed power generation

$$C_{DG1} = \sum_{i=1}^{N} E_{WT,i}\gamma_{WT} + \sum_{i=1}^{N} E_{PV,i}\gamma_{PV} \tag{31}$$

where $E_{WT,j}$ and $E_{PV,j}$ are the installed capacities of wind turbines and photovoltaic units at node $j$, respectively; $\gamma_{WT}$ and $\gamma_{PV}$ are the installation and construction costs of wind turbines and photovoltaic units per unit capacity, respectively; and $N$ is the number of nodes.

3. Micro turbine (MT) investment cost

$$C_{MT1} = \gamma_{MT}\sum_{j=1}^{N} E_{MT,j} \tag{32}$$

where $\gamma_{MT}$ is the unit capacity price of the MT, and $E_{MT,j}$ is the installed capacity of the gas turbine at node $j$.

4. Energy storage station (ESS) investment cost

$$C_{ESS1} = \sum_{j=1}^{N} (\gamma_{ESS}E_{ESSN,j} + \gamma_{PESS}P_{ESSN,j}) \tag{33}$$

where $\gamma_{ESS}$ is the price per unit capacity of energy storage, $\gamma_{PESS}$ is the price per unit power of energy storage, $E_{ESSN,j}$ is the installed capacity of ESS at node $j$, and $P_{ESSN,j}$ is the rated power of ESS at node $j$.

4.1.3. Annual Operation and Maintenance Cost $C_3$

$$C_3 = 365(C_{MT2} + C_{DG2} + C_{ESS2} + C_{EV2}) \tag{34}$$

where $C_{MT2}$ is the daily operating cost of the MT, $C_{DG2}$ is the daily operating cost of the distributed power source, and $C_{ESS2}$ is the daily operating cost of the energy storage. $C_{EV2}$ is the operation and maintenance costs of electric vehicle charging stations.

1. Daily operating cost of MT

$$C_{MT2} = \sum_{t=1}^{T}\sum_{j=1}^{N} (a_1 P_{MT,j,t}^2 + bP_{MT,j,t} + c) \tag{35}$$

where $a_1$, $b$, and $c$ are the operating cost coefficients of the MT, and $P_{MT,j,t}$ is the gas turbine output power at node $j$ during period $t$.

2. Daily operating cost of distributed power generation

Distributed power sources require regular maintenance during daily operation, so their operation and maintenance costs need to be considered.

$$C_{DG2} = \sum_{t=1}^{T} \sum_{j=1}^{N} (P_{WT2,j,t}\gamma_{WT2} + P_{PV2,j,t}\gamma_{PV2}) \tag{36}$$

where $\gamma_{WT2}$ and $\gamma_{PV2}$ are the operating costs per unit output power of the wind turbine and photovoltaic unit, respectively; and $P_{WT2,j,t}$ and $P_{PV2,j,t}$ are the total power output of the wind turbine and photovoltaic unit at node $i$ in period $t$, respectively.

3. Daily operating cost of energy storage

$$C_{ESS2} = \sum_{t=1}^{T} \sum_{j=1}^{N} P_{ESS,j,t}^2 \sigma_{ESS} \tag{37}$$

where $P_{ESS,j,t}$ is the energy storage power of node $j$ in period $t$, and $\sigma_{ESS}$ is the operation and maintenance cost coefficient of energy storage.

4. Operation and maintenance costs of electric vehicle charging stations

$$C_{EV2} = n_{EV}(\psi_1\gamma_{EV1} + \psi_2\gamma_{EV2}) \tag{38}$$

where $\psi_1$ is the number of inspections of a single charging pile, $\gamma_{EV1}$ is the single fee of a single charging pile, $\psi_2$ is the number of cleanings of a single charging pile, and $\gamma_{EV2}$ is the single cleaning fee of a single charging pile.

#### 4.1.4. Annual Carbon Emission Cost $C_4$

This paper introduces the carbon price growth rate to optimize the carbon trading model framework when calculating the carbon emission cost. Constructing a dynamically adjusted carbon price system guides entities in reducing carbon emissions through price signals.

1. Carbon quota model

There are two types of carbon emission sources in the distribution network: MT and power purchase from the upper main grid. The quota method used in this paper is a free quota.

$$P_{NET,t} = \sum_{j=1}^{N} (P_{Load,j,t} - P_{MT,j,t} - P_{WT,j,t} - P_{PV,j,t} - P_{ESS,j,t}) \tag{39}$$

$$\begin{cases} E_P = E_{MT} + E_{NET} \\ E_{MT} = \chi_m \sum_{t=1}^{T} \sum_{j=1}^{N} P_{MT,j,t} \\ E_{NET} = \chi_n \sum_{t=1}^{T} P_{NET,t} \end{cases} \tag{40}$$

where $E_P$, $E_{MT}$, and $E_{NET}$ are the carbon emission quotas of the distribution network, MT, and upper-level power purchase, respectively; $P_{NET,t}$ is the interactive power between the distribution network and the main grid during period $t$; $P_{Load,j,t}$ is the load power of node $j$ during period $t$; and $\chi_m$ and $\chi_n$ are the carbon emission quotas of unit

natural gas consumption of the gas turbine and unit electricity consumption of the main grid, respectively.

2. Actual carbon emission model

$$\begin{cases} E_{P,C} = E_{MT,C} + E_{NET,C} \\ E_{MT,C} = \sum_{t=1}^{T} \sum_{j=1}^{N} (\zeta_1 P_{MT,j,t}^2 + \zeta_2 P_{MT,j,t}) \\ E_{NET,C} = \varepsilon \sum_{t=1}^{T} (\mu_1 P_{NET,t}^2 + \mu_2 P_{NET,j}) \end{cases} \tag{41}$$

In the formula, $E_{P,C}$, $E_{MT,C}$, and $E_{NET,C}$ are the actual carbon emissions from the power distribution network, MT, and electricity purchases from upstream sources. $\zeta_1$ and $\zeta_2$ are the carbon emission coefficients of gas turbines, is the power share of thermal power plants in the interactive power, and $\mu_1$ and $\mu_2$ are the carbon emission coefficients of thermal power plants.

3. Optimized Stepped Carbon Emission Trading Model

By obtaining the carbon emission quota and actual carbon emissions of the distribution network, we can calculate the actual carbon emission trading amount in the carbon trading market.

$$\theta = E_{P,C} - E_P \tag{42}$$

where $\theta$ is the actual carbon emission trading amount of the distribution network.

$$\theta_{ex} = \begin{cases} A\theta & 0 < \theta \le d \\ (1+\alpha)A\theta & d < \theta \le 1.5d \\ (1+2\alpha)A\theta & 1.5d < \theta \le 5d \\ (1+3\alpha)A\theta & 5d < \theta \end{cases} \tag{43}$$

where $\theta_{ex}$ is the improved carbon emission cost, $A$ is the basic carbon emission price, $\alpha$ is the carbon price growth rate, and $d$ is the carbon price quota interval length.

### *4.2. Constraints*

#### 4.2.1. Power Flow Constraints and Safety Constraints of Distribution Networks

The power flow constraint equation contains quadratic terms and is nonlinear, making it difficult to solve directly. Therefore, the power flow model can be converted into a second-order cone programming model to achieve linearization. In this conversion process, the squared current term and the squared voltage term can be regarded as independent variables, thereby converting the original nonlinear optimization problem into a linear optimization problem that can be efficiently solved [41].

During the operation of the distribution network, it is necessary to ensure that each voltage level operates within a safe range. Since this paper adopts the second-order cone form for change, the voltage constraint adopts the square form:

$$U_{\min}^2 \le U_{j,t}^2 \le U_{\max}^2 \tag{44}$$

where $U_{i,t}$ is the operating voltage of node $j$ during period $t$, and $U_{\min}$ and $U_{\max}$ are the upper and lower limits of the node voltage, respectively.

The line transmission power is less than the maximum transmission power allowed by the line:

$$0 \leq I_{ij,t}^2 \leq I_{ij,\max}^2 \tag{45}$$

where $I_{ij,t}$ is the line current during period $t$, and $I_{ij,\max}$ is the maximum value of the line current.

#### 4.2.2. DG, MTs, and ESS Output Constraints

Distributed power sources and gas turbines have maximum output limits. Energy storage can not only store electrical energy but also release it. Therefore, the output of energy storage needs to meet the maximum and minimum output limits.

$$0 \leq P_{WT,j,t} \leq P_{WT,j,t,\max} \tag{46}$$

$$0 \leq P_{PV,j,t} \leq P_{PV,j,t,\max} \tag{47}$$

$$0 \leq P_{MT,j,t} \leq P_{MT,j,t,\max} \tag{48}$$

$$P_{ESS,j,t,\min} \leq P_{ESS,j,t} \leq P_{ESS,j,t,\max} \tag{49}$$

where $P_{WT,j,t,\max}$ is the maximum allowable output of the wind turbine at node $j$ during period $t$, $P_{PV,j,t,\max}$ is the maximum allowable output of the photovoltaic unit at node $j$ during period $t$, $P_{MT,j,t,\max}$ is the maximum allowable output of the MT at node $j$ during period $t$, and $P_{ESS,j,t,\min}$ and $P_{ESS,j,t,\max}$ are the minimum and maximum allowable outputs of the energy storage at node $j$ during period $t$, respectively.

### *4.3. Model Solution Method and Process*

For the comprehensive prediction system, we first collect regional historical meteorological data (wind speed, sunlight), EV quantity, type, and charging pile distribution data, and improve data quality through preprocessing. After the meteorological data are resampled by the sliding window method, it is fed into the improved LSTM neural network for iterative training to build a photovoltaic and wind turbine output prediction model. Based on the test set, the four-season output characteristics are generated to quantify the spatiotemporal distribution of renewable energy. At the same time, EV users are divided into fast charging and slow charging according to their charging behavior. Queuing theory and probability prediction models are used to simulate travel behavior and determine EV charging demand. Finally, the wind turbine, photovoltaic, and EV charging demands are output to the planning model together with the load and power output characteristics in the planning area as input.

For the planning model, the grid parameters (such as topology and load distribution) are initialized first, and the annual carbon emission quota and carbon trading price are set; the planning model including DG and energy storage units is solved with the objective function of minimizing economic cost, and its output strategy is adjusted dynamically; it is ensured that the actual carbon emissions meet the constraints through iterative optimization, and finally the wind turbine/photovoltaic access point and planned capacity, EV charging station site selection plan, ESS and MT output characteristics are output to build the distribution system planning model. The solution process is shown in Figure 3.

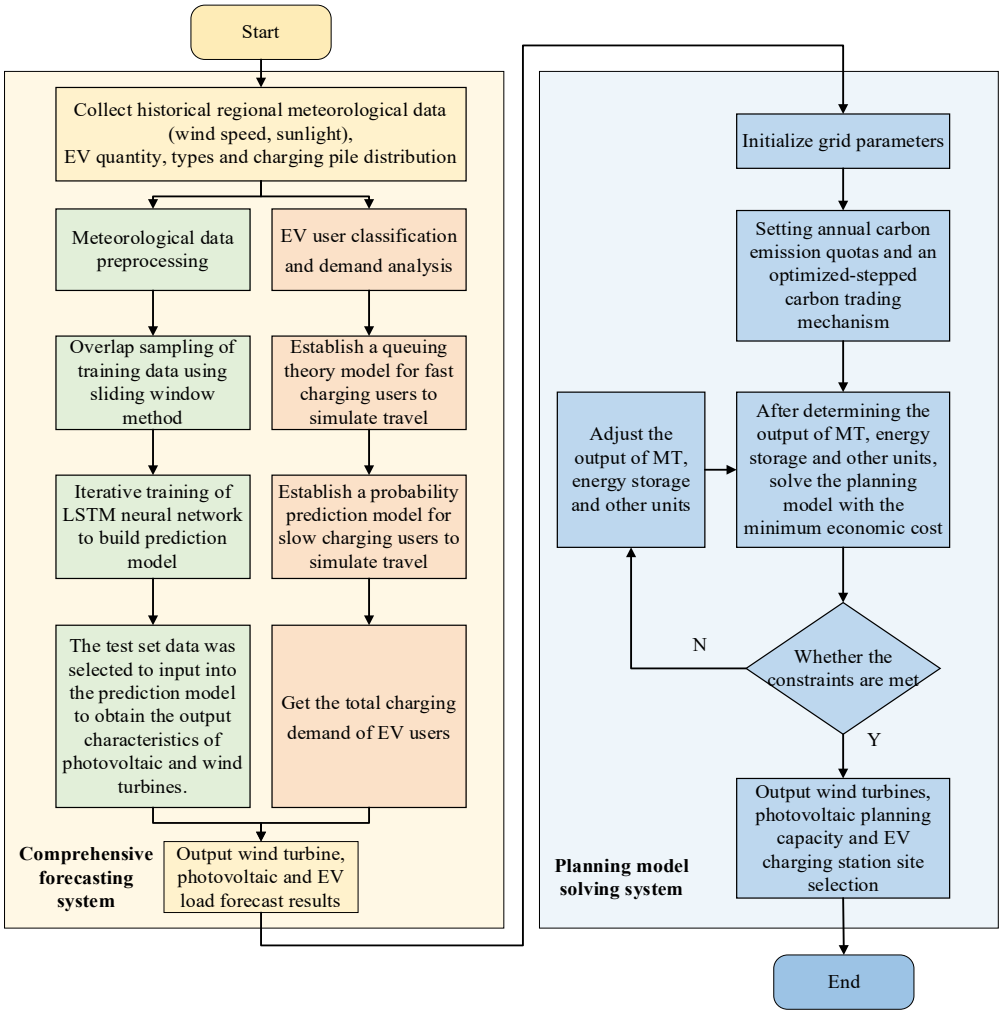


**Figure 3.** Solution process.

## 5. Case Analysis

This paper uses the operating data of DG and EVs in a certain region and the improved IEEE 33-node system for case analysis. The case study scenarios are designed to reflect realistic distribution network operations by adopting the IEEE 33-node system—a widely recognized benchmark with radial topology that accurately represents typical grid architectures. The historical wind speed, light intensity, temperature, humidity, and air pressure measurement data of a certain region are used for DG output modeling. The topology of the system is shown in Figure 4; the dotted lines in the figure represent candidate access nodes for the device, and the solid lines represent the determined site selection nodes for the device. The reference voltage per unit value of each node in the system is 1, and the peak value of the basic active load of the network is 3715 kW. For the EV centralized fast-charging station, four DC fast chargers (3C charging standard) are configured, with a single machine rated power of 175 kW. The optional station sites are nodes 11 and 29. There are 500 electric private cars in the regional EV slow-charging users, all of which use AC slow-charging piles with a rated charging power of 7 kW. The power loss of electric private cars per 100 km is 14 kWh, which is distributed in four large residential areas at nodes 16, 21, 24, and 31. The installed capacity of MT is 500 kW, ESS is a battery energy storage system, the rated parameter is 200 kW/800 kWh, and the charge–discharge energy conversion efficiency is 0.95. MT is connected to node 16, and ESS is connected to node 7. In addition, the optional sites for wind turbines are nodes 8, 14, and 29, and the optional sites for photovoltaics are nodes 4, 19, and 23. The upper limits of the total installed capacity of wind turbines and

photovoltaics are 1000 kW and 1500 kW, respectively. The carbon price growth rate $\alpha$ is 0.2, and the carbon price quota interval length $d$ is 10 t. The typical daily load characteristic curve in the example system is shown in Figure 5, and the time-of-use electricity price characteristic curve is shown in Figure 6. Parameters are detailed in Table 1 [19].

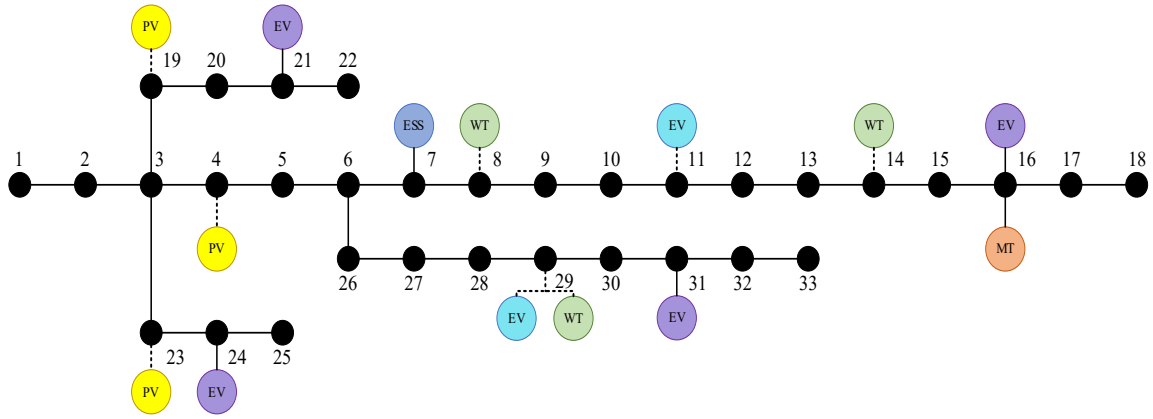


**Figure 4.** IEEE33 node system schematic.

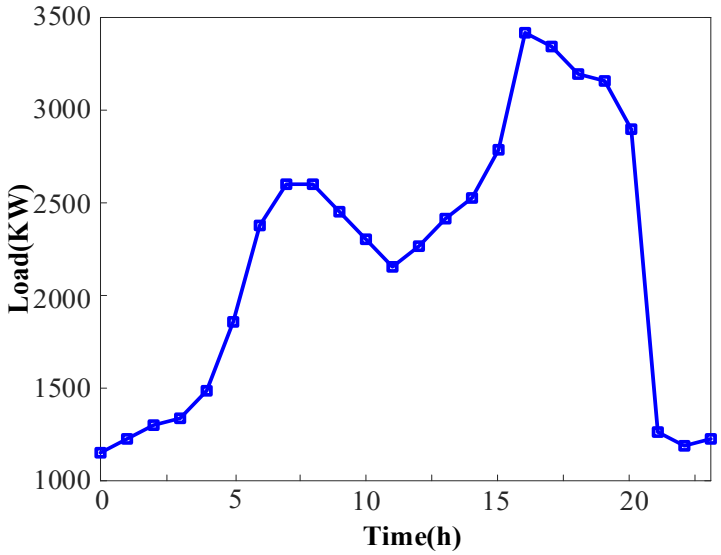


**Figure 5.** Typical daily load characteristic curve.

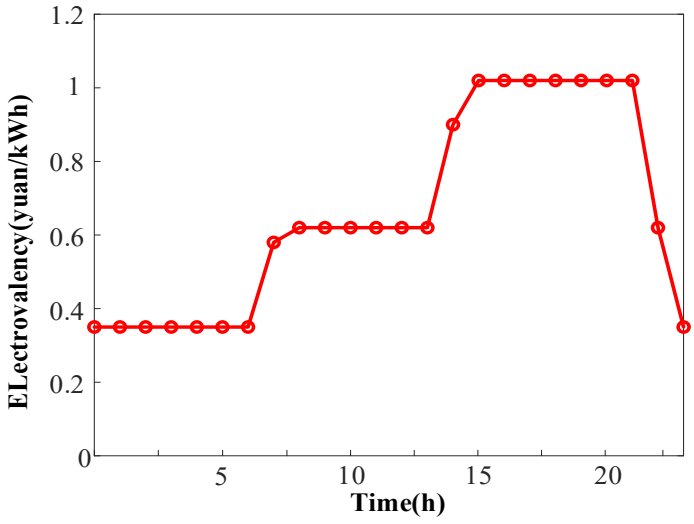


**Figure 6.** Time-of-use electricity price characteristic curve.

**Table 1.** Specific parameters in the case study.

| Serial Number | Device Name | Value |
|---|---|---|
| 1 | EV DC fast charger | 175 kW |
| 2 | EVAC slow-charging pile | 7 kW |
| 3 | MT | 500 kW |
| 4 | ESS | 200 kW |
| 5 | Wind turbines | 1000 kW |
| 6 | Photovoltaic | 1500 kW |
| 7 | Carbon price growth rate $\alpha$ | 0.2 |
| 8 | Carbon price quota interval length $d$ | 10 t |

### *5.1. Build a Predictive Model*

This paper selects relevant historical data of a certain area as the test system. The measurement data interval is 15 min, including historical data of five indicators: wind speed, light intensity, temperature, humidity, and air pressure. The data from August 2019 is used for training and testing. The first 80% of the data in the entire data set is used as the training set, and the last 20% is used as the test set. The prediction results of wind speed and light intensity are shown in Figure 7.

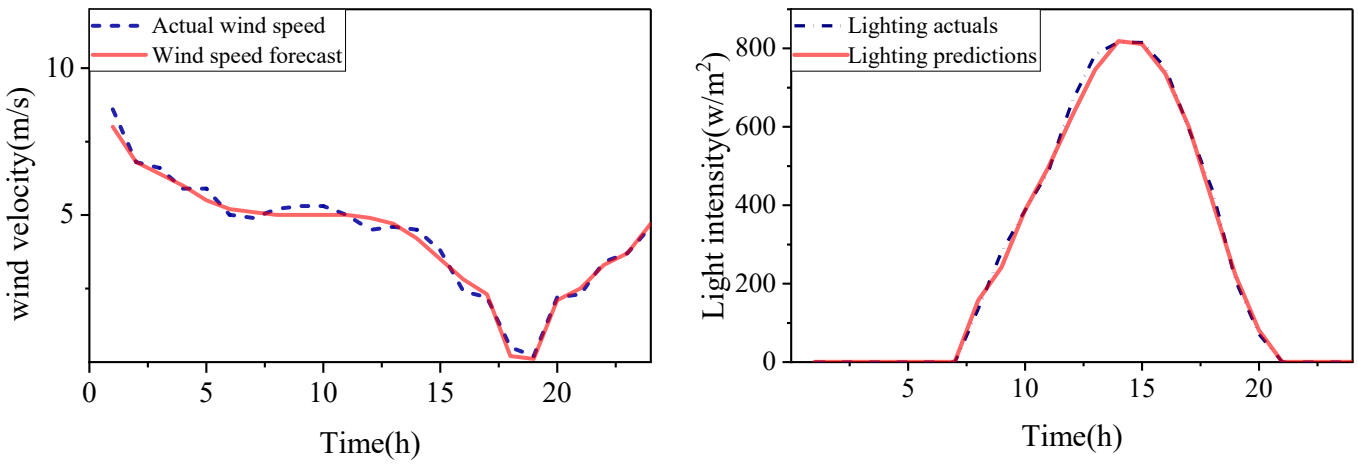


**Figure 7.** Comparison of wind speed and light intensity predictions.

As illustrated in Figure 7, the proposed prediction model demonstrates robust performance throughout the 24-h forecasting horizon. Specifically, the model achieves a wind speed prediction accuracy with RMSE of 0.26, MAE of 0.21, and SMAPE of 10.78%. For solar irradiance forecasting, the performance metrics yield RMSE of 16.44, MAE of 9.51, and SMAPE of 3.06%. The LSTM is a basic model and is often used for prediction. The wind speed and solar irradiance are also predicted by the LSTM model. Specifically, the model achieves a wind speed prediction accuracy with RMSE of 0.59, MAE of 0.47, and SMAPE of 19.17%. For solar irradiance forecasting, the performance metrics yield RMSE of 42.18, MAE of 25.24, and SMAPE of 10.63%. Notably, the CEEMDAN-LSTM model exhibits exceptional performance in predicting peak irradiance during noontime periods.

By substituting the wind speed and solar irradiance results obtained from the prediction model into the wind speed Weibull distribution model and the photovoltaic Beta distribution model, the output characteristic curve of DG can be calculated as shown in Figure 8.

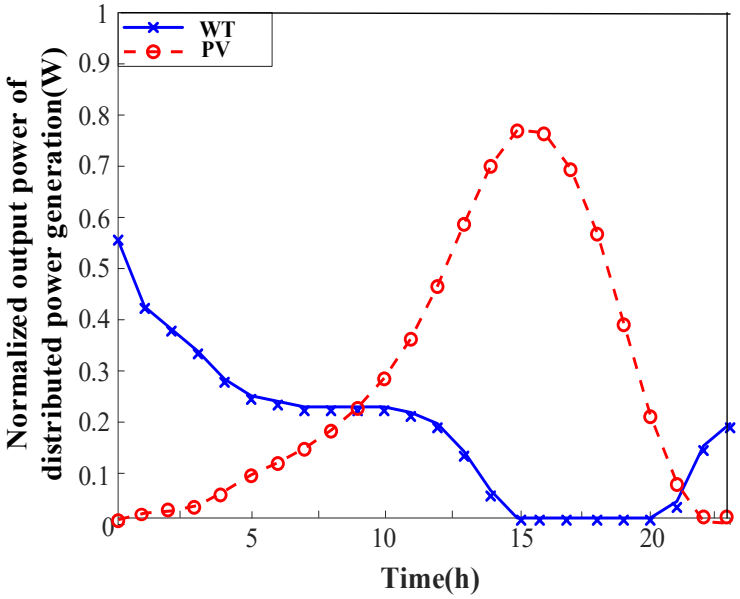


**Figure 8.** DG output characteristic curve.

*5.2. EV Load Forecasting*

Combined with the contents of Section 3.1 of this paper, the load demand prediction models for EV fast-charging stations and EV slow-charging users are constructed. Under the corresponding conditions set in the example, the EV load prediction curve is shown in Figure 9.

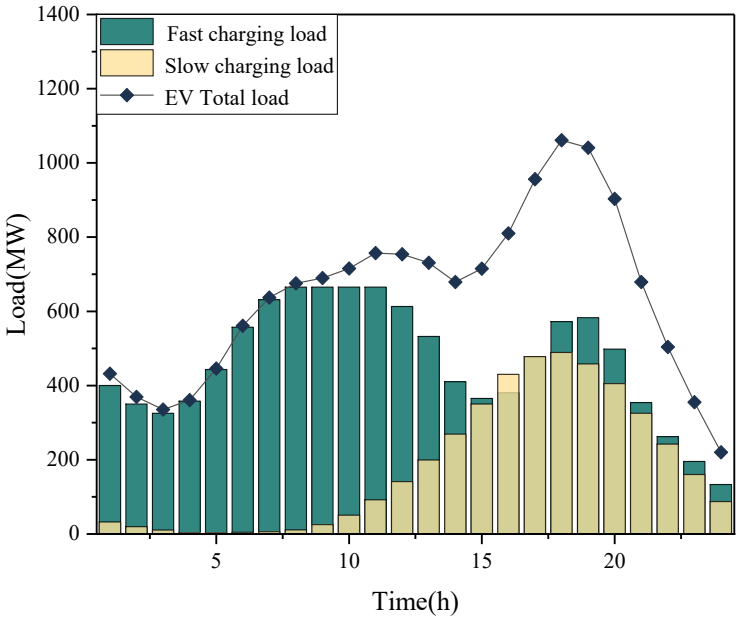


**Figure 9.** EV load forecast.

The EV load forecasting results reveal distinct characteristics between fast-charging and slow-charging loads. Fast-charging users in this study primarily consist of operational vehicles such as electric taxis and ride-hailing cars, which exhibit significantly different usage patterns compared to private passenger vehicles. Night-shift taxis typically complete their operations and undergo driver shift changes between 8:00 and 10:00. In the proposed model, the taxi shift-change period ($t_e$) is incorporated into the Poisson arrival rate $\xi$, reflecting the reality that many vehicles enter charging stations simultaneously during shift transitions. Unlike private vehicles, operational vehicles must replenish their battery

before commencing their workday to ensure sufficient driving range. As a result, the peak in charging demand does not coincide with peak traffic flow. Moreover, the fast-charging load exhibits a pronounced bimodal distribution, with peak demand occurring during 8:00–10:00 and 18:00–20:00, coinciding with commuting rush hours. This pattern reflects fast-charging users' preference for concentrated charging before and after daily commutes. The slow-charging load curve corresponds to the charging habits of residents during nighttime parking. The combined charging load, formed by superimposing fast and slow-charging demands, reaches its peak during evening rush hours and trough in early morning hours. When further superimposed with conventional residential loads, this combined demand profile significantly elevates grid peak loads, thereby exacerbating the risks of local grid overload.

### *5.3. Analysis of Planning Results*

Combining the planning model established in the previous article and solving it according to the process of 3.3, the planning model solution results are shown in Table 2.

**Table 2.** Planning solution results.

| Serial Number | Designation | Cost (Ten Thousand Yuan RMB) |
|---|---|---|
| 1 | Total annual cost | 4337.82 |
| 2 | Annual investment cost | 2480 |
| 3 | Annual operation and maintenance cost | 333.42 |
| 4 | Annual carbon emissions cost | 1400.8 |
| 5 | Annual electricity purchase cost | 123.6 |

After introducing the carbon pricing optimization mechanism, the model is solved, and the optimization results are obtained. The wind power installed capacities of nodes 14 and 29 are 107 kW and 893 kW, respectively; the photovoltaic installed capacities of nodes 4, 19, and 23 are 607 kW, 428 kW, and 466 kW, respectively; the EV centralized charging station is configured at node 29; the MT installation node is at 16, with an installed capacity of 500 kW; the ESS installation node is at 7, with an installed capacity of 800 kWh. Thus, some optimization results are obtained. Under this planning, it can meet user needs and minimize the total annual cost. The power purchased by the upper main grid is shown in Figure 10, the MT output is shown in Figure 11, and the relationship between the ESS charging and discharging power and the amount of electricity is shown in Figure 12.

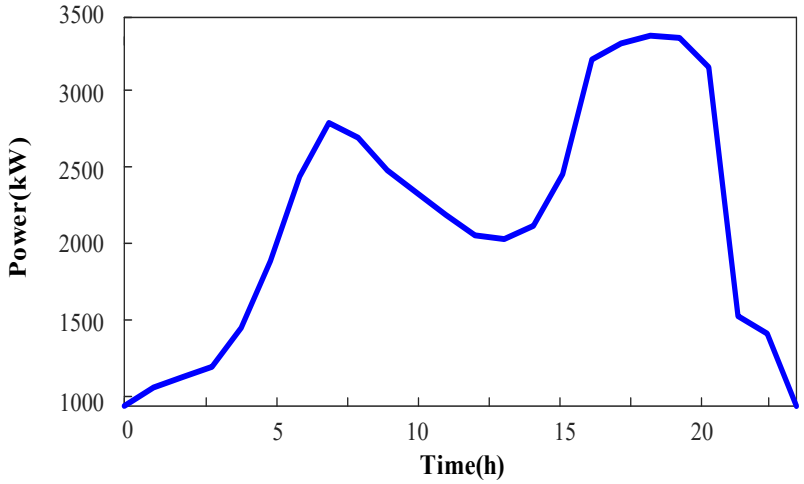


**Figure 10.** Bulk power purchase curve.

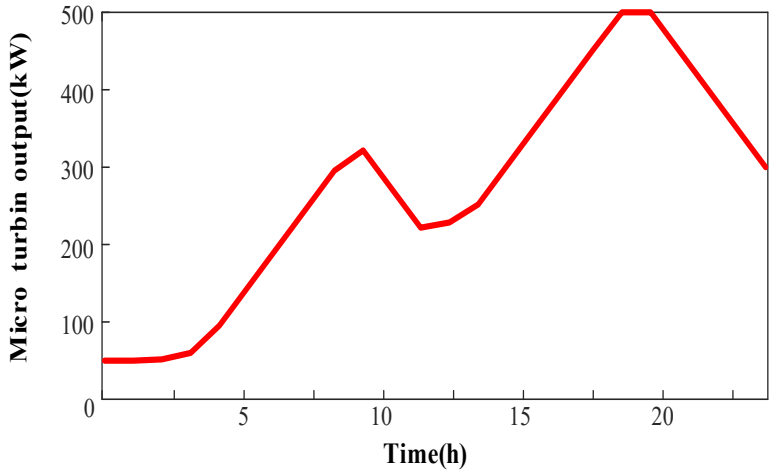


**Figure 11.** MT output.

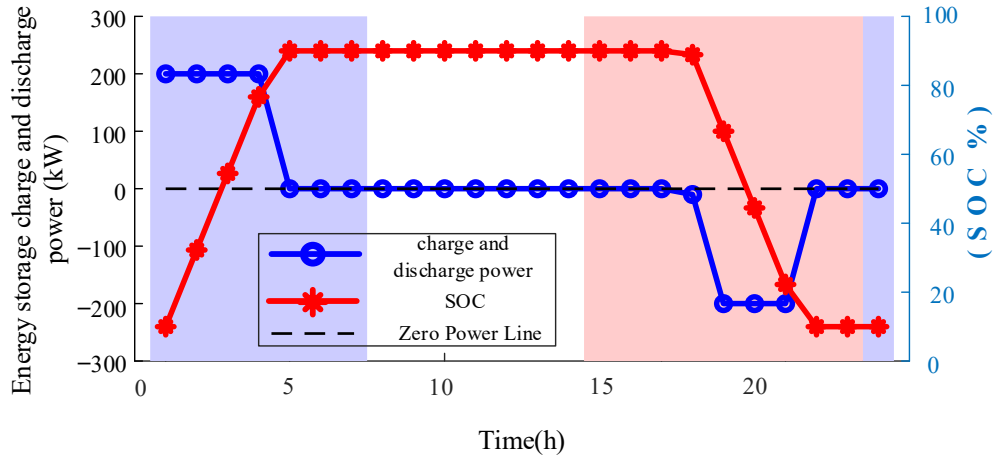


**Figure 12.** Relationship between energy storage charging and discharging power and power.

As shown in Figure 10, the trend of the bulk power purchase curve closely aligns with the load curve. When the load is low, renewable energy sources and gas turbines provide auxiliary power output, resulting in a lower bulk power purchase. During peak load periods, the distribution grid primarily relies on bulk power purchase to meet demand. Figure 11 illustrates that the output of the MT is influenced by both the load curve and time-of-use (TOU) electricity pricing. When the load increases or electricity prices are high, the MTs operate at full capacity, reducing bulk power purchase and thereby indirectly lowering electricity procurement costs. From Figure 12, it can be observed that the ESS operates under the dual constraints of TOU pricing and carbon emission costs. The ESS charges when electricity prices are low and discharges during periods of high electricity prices and elevated carbon costs. This strategy reduces bulk power purchase, enabling the distribution grid to indirectly minimize carbon emission costs. The real-time electricity prices and carbon prices guide dynamic ESS charging/discharging, while the dynamic carbon pricing mechanism, in turn, optimizes ESS capacity planning and siting. Through this synergistic mechanism, conventional peak-shaving functions are achieved while creating a new pathway for reducing system emissions by displacing high-carbon grid power. This innovation enables planning solutions to automatically adapt to dynamic changes in electricity and carbon markets, providing new insights for the low-carbon transformation of distribution networks.

Figure 13 shows the power balance diagram of the distribution grid system. The upper section represents the power demand side, including ESS charging, network losses,

and system load demand. The lower section depicts the power supply side, consisting of wind/PV generation, MT output, ESS discharging, and power purchased from the main grid. As evident from the figure, the system maintains power balance over the 24-h period, with total load demand matching total power supply. Renewable generation forecasts guide optimal charging station siting. Dynamic carbon pricing adjusts based on real-time emission levels, creating economic incentives for load-renewable energy coordination. The joint optimization framework iteratively balances these components under technical constraints.

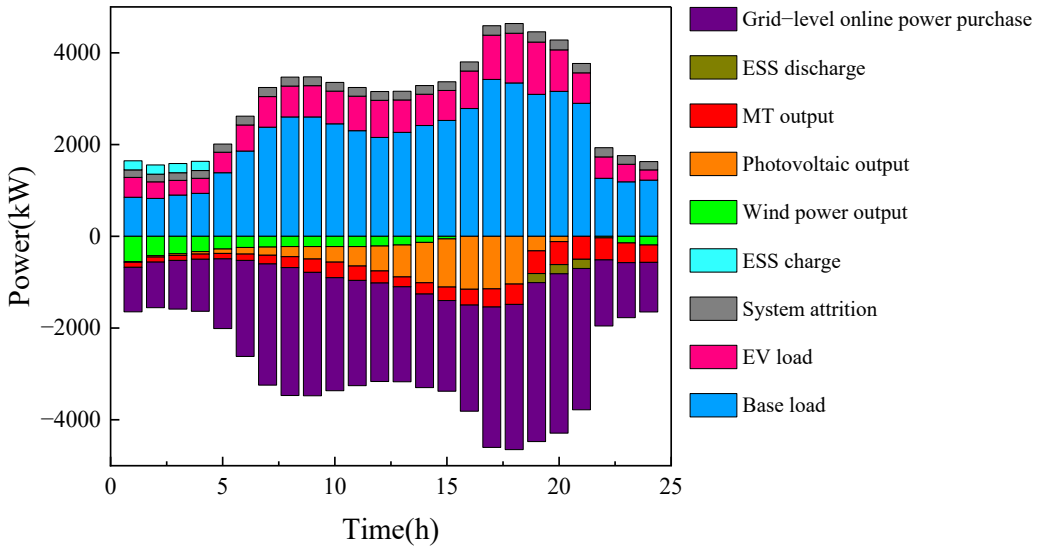


**Figure 13.** Power balance diagram.

## 6. Conclusions

This study presents an innovative integrated planning framework that systematically coordinates renewable energy deployment, EV charging infrastructure optimization, and carbon-aware operation strategies. The key methodological advances include: (1) a hybrid forecasting approach combining signal decomposition and deep learning for improved renewable energy prediction; (2) behaviorally grounded EV charging models that distinguish between fast- and slow-charging patterns; and (3) a dynamic carbon pricing mechanism that aligns economic incentives with emission reduction targets. By jointly optimizing these interconnected systems, the framework provides a comprehensive solution for power distribution planning in the context of energy transition, enabling effective coordination between renewable integration, transportation electrification, and carbon mitigation strategies. The carbon-aware planning methodology intrinsically links infrastructure deployment decisions with emission reduction objectives, where renewable energy penetration directly offsets fossil-fueled generation while optimally located EV stations reduce unnecessary grid reinforcement needs. This systems approach ensures that all planning elements—from renewable capacity sizing to charging infrastructure placement—work in concert to achieve the tripartite goals of reliability assurance, cost efficiency, and carbon mitigation, with their interrelationships thoroughly discussed through the lens of integrated energy-transportation system operation. The core method proposed in this study can adapt to the development of regional power grids or the evolution of electric vehicle technology.

## 7. Discussion

This study provides a comprehensive framework for the joint planning of renewable energy and electric vehicle charging stations. Although this study establishes a theoretical framework and preliminary validation, in subsequent research, it will be systematically compared with existing planning methods in terms of cost savings, emission reduction,

and renewable energy utilization, and a systematic sensitivity analysis will be conducted to evaluate how the uncertainty of carbon pricing schemes and renewable energy forecasts affects planning results. The robustness of this method under extreme conditions of renewable energy and EV loads is discussed, and several important directions for future research are identified. Several important directions for future research have been identified:

Firstly, although our current electric vehicle charging model distinguishes between fast- and slow-charging behaviors, future research will incorporate more refined classifications of electric vehicles, and the impact of climate factors on electric vehicle charging behavior should be considered. To better capture the diversity of charging in the real world. This expansion will provide more tailored infrastructure planning for different user groups.

Secondly, we will expand the evaluation of dynamic carbon pricing mechanisms for different market configurations to assess their adaptability to different policy environments. This analysis will provide practical insights for implementing carbon awareness planning in different regulatory contexts.

Thirdly, there are several technological limitations worth further investigation: (1) the impact of communication delays on real-time carbon price signals, (2) the development of dynamic V2G models that incorporate battery degradation and user incentives, and (3) enhanced prediction techniques for extreme climate events. These improvements will be combined with sensitivity analysis of the system to quantify how uncertainty in carbon pricing and renewable energy forecasting affects planning outcomes.

**Author Contributions:** Conceptualization, S.W.; methodology, B.F.; software, J.Z.; validation, Z.C.; supervision and methodology, M.W.; writing—review and editing, H.X.; writing—original draft, M.J. All authors have read and agreed to the published version of the manuscript.

**Funding:** This paper is funded by the Science and Technology Project of China Southern Power Grid Company Limited (grant number: 070000KC23110018).

**Data Availability Statement:** Publicly available datasets are analyzed in this study.

**Conflicts of Interest:** Authors Shanli Wang, Bing Fang, Jiayi Zhang, Zewei Chen, Mingzhe Wen and Huanxiu Xiao wrer employed by the company Hainan Power Grid Co., Ltd. The remaining authors declare that the research was conducted in the absence of any commercial or financial relationships that could be construed as a potential conflict of interest.

## References

1. Guler, N.; Ismail, Z.M.; Ben Hazem, Z.; Naik, N. Adaptive fuzzy logic controller-based intelligent energy management system scheme for hybrid electric vehicles. *IEEE Access* **2024**, *12*, 173441–173454. [CrossRef]
2. Doosti, R.; Rezazadeh, A.; Sedighizadeh, M. Power and energy management strategies for a microgrid with the presence of electric vehicles and caes considering the uncertainty of resources. *Processes* **2023**, *11*, 1156. [CrossRef]
3. Li, X.J.; Qian, J.X.; Yang, C.H.; Chen, B.Y.; Wang, X.; Jiang, Z.N.; Bak, C.L. New Power System Planning and Evolution Path with Multi-Flexibility Resource Coordination. *Energies* **2024**, *17*, 273. [CrossRef]
4. Huang, Z.T.; Xu, Y.H.; Chen, L.; Ye, X.J. Coordinated planning method considering flexible resources of active distribution network and soft open point integrated with energy storage system. *Iet Gener. Transm. Distrib.* **2023**, *17*, 5273–5285. [CrossRef]
5. Wang, Y.; Li, J. Optimizing multi-energy systems with enhanced robust planning for cost-effective and reliable operation. *Int. J. Electr. Power Energy Syst.* **2024**, *161*, 110178. [CrossRef]
6. Fang, Y.; Fan, R.X.; Liu, Z.H. A study on the energy storage scenarios design and the business model analysis for a zero-carbon big data industrial park from the perspective of source-grid-load-storage collaboration. *Energy Rep.* **2023**, *9*, 2054–2068. [CrossRef]
7. Zhang, Y.J.; Yang, X.A.; Fang, L.R.; Lyu, Y.; Xiong, X.J.; Zhang, Y.F. Data-driven day-ahead dispatch method for grid-tied distributed batteries considering conflict between service interests. *Electronics* **2024**, *13*, 4357. [CrossRef]
8. Heng, S.; Lurui, F.; Xiaoyang, C.; Chenghong, G.; Kang, M.; Xinsong, Z.; Zhong, Z.; Juping, G.; Eng Gee, L. Review of the opportunities and challenges to accelerate mass-scale application of smart grids with large-language models. *IET Smart Grid* **2024**, *7*, 737–759.

9. Jakoplic, A.; Frankovic, D.; Kirincic, V.; Plavsic, T. Benefits of short-term photovoltaic power production forecasting to the power system. *Optim. Eng.* **2021**, *22*, 9–27. [CrossRef]
10. Dong, Y.X.; Ma, S.D.; Zhang, H.C.; Yang, G.H. Wind Power Prediction Based on Multi-class Autoregressive Moving Average Model with Logistic Function. *J. Mod. Power Syst. Clean Energy* **2022**, *10*, 1184–1193. [CrossRef]
11. Cunha, J.L.R.N.; Pereira, C.M.N.A. A hybrid model based on STL with simple exponential smoothing and ARMA for wind forecast in a Brazilian nuclear power plant site. *Nucl. Eng. Des.* **2024**, *421*, 113026. [CrossRef]
12. Wu, Q.L.; Lin, H.X. Short-Term Wind Speed Forecasting Based on Hybrid Variational Mode Decomposition and Least Squares Support Vector Machine Optimized by Bat Algorithm Model. *Sustainability* **2019**, *11*, 652. [CrossRef]
13. Park, S.; Jung, S.L.Y.; Lee, J.G.; Hur, J. A Short-Term Forecasting of Wind Power Outputs Based on Gradient Boosting Regression Tree Algorithms. *Energies* **2023**, *16*, 1132. [CrossRef]
14. Wang, Z.J.; Zhang, J.; Zhang, Y.; Huang, C.; Wang, L. Short-Term Wind Speed Forecasting Based on Information of Neighboring Wind Farms. *IEEE Access* **2020**, *8*, 16760–16770. [CrossRef]
15. Wu, H.J.; Meng, K.Q.L.; Fan, D.E.R.; Zhang, Z.Q.; Liu, Q. Multistep short-term wind speed forecasting using transformer. *Energy* **2022**, *261*, 125231. [CrossRef]
16. Araya, I.A.; Valle, C.; Allende, H. A Multi-Scale Model based on the Long Short-Term Memory for day ahead hourly wind speed forecasting. *Pattern Recognit. Lett.* **2020**, *136*, 333–340. [CrossRef]
17. Yi, T.; Zhang, C.; Lin, T.Y.; Liu, J.P. Research on the spatial-temporal distribution of electric vehicle charging load demand: A case study in China. *J. Clean. Prod.* **2020**, *242*, 118457. [CrossRef]
18. Das, H.S.; Rahman, M.M.; Li, S.; Tan, C.W. Electric vehicles standards, charging infrastructure, and impact on grid integration: A technological review. *Renew. Sustain. Energy Rev.* **2020**, *120*, 109618. [CrossRef]
19. Wu, Y.; Dong, Z.; Zhao, Y.; Chu, Y. Joint optimization planning of distribution network DG and EV charging station based on LSTM algorithm. *Electr. Supply* **2023**, *40*, 64–74.
20. Wang, S.Q.; Liu, B.; Li, Q.Y.; Han, D.; Zhou, J.S.; Xiang, Y. EV Charging Behavior Analysis and Load Prediction via Order Data of Charging Stations. *Sustainability* **2025**, *17*, 1807. [CrossRef]
21. Xing, Y.; Li, F.; Sun, K.; Wang, D.; Chen, T.Y.; Zhang, Z. Multi-type electric vehicle load prediction based on Monte Carlo simulation. *Energy Rep.* **2022**, *8*, 966–972. [CrossRef]
22. Yang, J.; Wu, F.Z.; Yan, J.; Lin, Y.J.; Zhan, X.P.; Chen, L.; Liao, S.Y.; Xu, J.; Sun, Y.Z. Charging demand analysis framework for electric vehicles considering the bounded rationality behavior of users. *Int. J. Electr. Power Energy Syst.* **2020**, *119*, 105952. [CrossRef]
23. Stenstadvolden, A.; Stenstadvolden, O.; Zhao, L.; Kapourchali, M.H.; Zhou, Y.H.; Lee, W.J. Data-Driven Analysis of a NEVI-Compliant EV Charging Station in the Northern Region of the US. *IEEE Trans. Ind. Appl.* **2024**, *60*, 5352–5361. [CrossRef]
24. Fang, X.; Wang, B.B.; Cao, W.J. A Day-Ahead Peak Shaving Strategy Using Data-Driven Prediction of EV Charging Behavior. *J. Electr. Eng. Technol.* **2025**, *20*, 2901–2928. [CrossRef]
25. Niu, H.N.; Yang, L.; Zhao, J.X.; Wang, Y.Z.; Wang, W.Z.; Liu, F.C. Flexible-regulation resources planning for distribution networks with a high penetration of renewable energy. *Iet Gener. Transm. Distrib.* **2018**, *12*, 4099–4107.
26. Kothona, D.; Bouhouras, A.S. A Two-Stage EV Charging Planning and Network Reconfiguration Methodology towards Power Loss Minimization in Low and Medium Voltage Distribution Networks. *Energies* **2022**, *15*, 3808. [CrossRef]
27. Liu, L.J.; Xie, F.; Huang, Z.L.; Wang, M.Q. Multi-Objective Coordinated Optimal Allocation of DG and EVCSs Based on the V2G Mode. *Processes* **2021**, *9*, 18. [CrossRef]
28. Zhang, Y.; Ai, X. A distribution network planning method that considers the uncertainty and correlation of wind and solar output. *Mod. Electr. Power* **2024**, *41*, 318–325.
29. Feng, Y.; Ying, Z.F.; Yan, J.H. Optimize the operation of multi-energy complementary micro-energy grid energy storage devices considering carbon emission costs. *Power Syst. Prot. Control* **2021**, *49*, 92–99.
30. Peng, J.; Wang, J.; Qi, F.J.; Liao, Y.X. Multi-stage expansion planning of a distribution network with double-carbon policy. *Power Syst. Prot. Control* **2022**, *50*, 153–161.
31. Chen, J.P.; Hu, Z.J.; Chen, Y.G.; Chen, J.B.; Chen, W.N.; Gao, M.X.; Lin, M.R.; Du, Y.X. Thermoelectric optimization of integrated energy system considering ladder-type carbon trading mechanism and electric hydrogen production. *Electr. Power Autom. Equip.* **2021**, *41*, 48–55.
32. Yan, N.; Ma, G.C.; Li, X.J.; Guerrero, J.M. Low-Carbon Economic Dispatch Method for Integrated Energy System Considering Seasonal Carbon Flow Dynamic Balance. *IEEE Trans. Sustain. Energy* **2023**, *14*, 576–586. [CrossRef]
33. Chen, L.Y.; Liu, X.; Zeng, C.; He, X.Z.; Chen, F.G.; Zhu, B.S. Temperature Prediction of Seasonal Frozen Subgrades Based on CEEMDAN-LSTM Hybrid Model. *Sensors* **2022**, *22*, 5742. [CrossRef]
34. Cai, H.H.; Wu, Z.H.; Huang, C.; Huang, D.Z. Wind Power Forecasting Based on Ensemble Empirical Mode Decomposition with Generalized Regression Neural Network Based on Cross-Validated Method. *J. Electr. Eng. Technol.* **2019**, *14*, 1823–1829. [CrossRef]

35. Liang, C.H.; Ren, W.H.; Cheng, P.; Ding, C. Control Strategy of Photovoltaic DC Microgrid Based on Fuzzy EEMD. *Teh. Vjesn.-Tech. Gaz.* **2022**, *29*, 1762–1769.
36. Ji, M.; Zhao, X.Y.; Zhu, W.; You, Y.C.; Zhang, J.F.; Shang, M.; Chuai, X.; Xue, Y.J.; Lian, C.H.; Chen, W. Noise Attenuation Using Adaptive Wavelet Threshold Based on Ceemd Inf-X Domain. *J. Seism. Explor.* **2023**, *32*, 131–153.
37. Guo, C.; Kang, X.M.; Xiong, J.P.; Wu, J.H. A New Time Series Forecasting Model Based on Complete Ensemble Empirical Mode Decomposition with Adaptive Noise and Temporal Convolutional Network. *Neural Process. Lett.* **2023**, *55*, 4397–4417. [CrossRef]
38. Jiang, W.; Cheng, Y.; Yan, Z.; Feng, D.H. Reliability-constrained dynamic economic dispatch of power system with wind farms. *Electr. Power Autom. Equip.* **2013**, *33*, 27–33.
39. Tian, L.T.; Shi, S.L.; Jia, Z. A Statistical Model for Charging Power Demand of Electric Vehicles. *Power Syst. Technol.* **2010**, *34*, 126–130.
40. Guo, C.X.; Liu, D.Y.; Zhu, C.Z.; Wang, X.P.; Cao, X. Modeling and analysis of electric vehicle charging load in residential area. *Electr. Power Autom. Equip.* **2020**, *40*, 394–402.
41. Taylor, J.A.; Hover, F.S. Convex Models of Distribution System Reconfiguration. *IEEE Trans. Power Syst.* **2012**, *27*, 1407–1413. [CrossRef]


**Disclaimer/Publisher's Note:** The statements, opinions and data contained in all publications are solely those of the individual author(s) and contributor(s) and not of MDPI and/or the editor(s). MDPI and/or the editor(s) disclaim responsibility for any injury to people or property resulting from any ideas, methods, instructions or products referred to in the content.